Extension of Soft-Switching Region of Dual-Active-Bridge Converter by a Tunable Resonant Tank

M. Yaqoob, *Student Member, IEEE*, K. H. Loo, *Member, IEEE*, and Y. M. Lai, *Senior Member, IEEE*

***Abstract*—Hard-switching-induced switching loss can contribute significantly to the power loss of an isolated bidirectional dual-active-bridge (DAB) dc–dc converter operating at high frequency. An LC-type series resonant DAB converter based on a switch-controlled-inductor (SCI) is proposed to mitigate the loss arising from hard switching under wide-range variations in output voltage and current. Zero-voltage switching is achieved at the primary side (high voltage), while at the secondary side (low voltage), zero-current switching is preferred to reduce excessive ringing due to circulating current and switching loss. In order to achieve reduced conduction loss, a nominal operating point is chosen where the root-mean-square resonant tank current is the minimum. To validate the proposed topology and modulation scheme, an LC-type series resonant DAB converter based on SCI operating at 100 kHz is designed to interface a 400-V dc bus to a supercapacitor-based energy storage. Simulation and experimental results validate the effectiveness of the proposed topology for charging/discharging a supercapacitor with an output voltage variation of between 10 and 48 V and a maximum rated power of 480 W. A maximum efficiency of 94.6% is achieved using the proposed topology and modulation scheme.**

***Index Terms*—Dual-active-bridge (DAB) converter, supercapacitor, switch-controlled inductor, zero-current switching (ZCS), zero-voltage switching (ZVS).**

I. Introduction

BIDIRECTIONAL power flow is expected to be an essential feature in future electric power systems where bidirectional power conversion systems play a significant role. The increasing penetration of renewable energy generation arises due to its positive impact on the environment by providing low carbon emissions and this has led to the development of microgrid systems [1], [2]. A generic microgrid system is mainly composed of distributed renewable energy resources and storages as shown in Fig. 1. These renewable energy resources

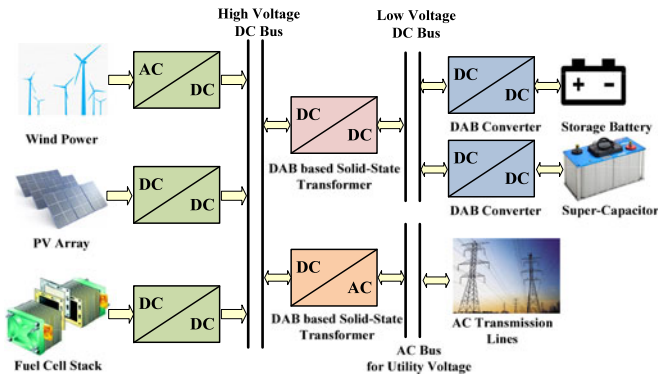

Fig. 1. Bidirectional power flow and distributed generation in a microgrid system.

are highly dynamic in nature and need to be equipped with energy storages to achieve stable and uninterruptible power supply. Bidirectional power conversion systems can be used to integrate these storage devices to the dc bus in a microgrid and in this context many bidirectional power converters have been proposed. Dual-active-bridge (DAB) converter has shown many advantages over its counterpart topologies in terms of device stress, ease of control, galvanic isolation, and power density. It was first proposed in [3] and with recent advancements in semiconductor and magnetic devices it has attracted more attention for its use in medium-voltage microgrid systems [4]–[7]. A DAB converter based on the LC-type series resonant tank uses an inductor and a capacitor as energy transfer elements [8], but under wide variations in output voltage and current, this topology undergoes hard switching in certain operating regions and causes switching loss that deteriorates converter's performance in terms of efficiency. Hard switching in the conventional DAB converter is mainly due to the out-of-phase relationship between the series resonant tank's current and bridge voltages [9]. There is an increase in the trend of high-frequency operation of the DAB converter due to the rise of new semiconductor devices with extremely low gate charge such as SiC (Silicon-Carbide) and GaN (Gallium-Nitride) [11], [12]. When operating at high frequencies, these devices can suffer from excessive switching loss.

Many modulation methods and converter topologies have been proposed to extend soft-switching region but they cover

Manuscript received September 21, 2016; revised November 13, 2016; accepted January 3, 2017. Date of publication January 17, 2017; date of current version August 2, 2017. This work was supported by the University Grants Committee of the Hong Kong Special Administrative Region, Research Grants Council, under Early Career Scheme (ECS) PolyU 5390/13E. Recommended for publication by Associate Editor R. Ayyanar.

The authors are with the Department of Electronic and Information Engineering, The Hong Kong Polytechnic University, Hong Kong (e-mail: muhammad.yaqoob@connect.polyu.hk; kh.loo@polyu.edu.hk; enymlai@polyu.edu.hk).

Color versions of one or more of the figures in this paper are available online at http://ieeexplore.ieee.org.

Digital Object Identifier 10.1109/TPEL.2017.2654505

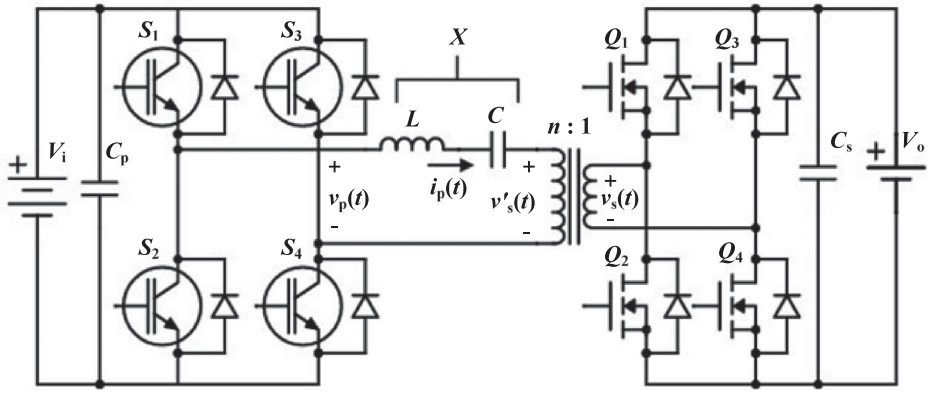

Fig. 2. Conventional DAB converter based on an LC-type series resonant tank.

only limited operating regions. Single-phase-shift modulation is used in [8] for the design of the LC-type series resonant DAB converter. It uses one degree of freedom to modulate power and fails to provide full-range soft switching especially under light-load condition and nonunity voltage gain operation. In order to reduce circulating current, an extended-phase-shift (EPS) modulation is introduced in [13]–[15], which uses an internal-phase-shift within the primary or secondary bridges, and an external-phase-shift between the primary and secondary bridges of a DAB converter for power modulation. Investigation of zero-voltage switching (ZVS) and non-ZVS operating regions under dual-phase-shift (DPS) modulation has been presented in [16] and is implemented in [17]–[19]. Power characterization of a DAB converter using triple-phase-shift (TPS) is presented in [20]–[22]. With EPS, DPS, and TPS, however, soft switching can only be achieved for certain operating regions and also at the cost of complex modulation schemes. Fundamental duty modulation (FDM) and fundamental-optimal strategy based on fundamental component analysis (FCA) are explained in [23] and [24], which also achieve ZVS of all switches under certain operating regions only. The main objective of FDM based on FCA is to reduce circulating current and computational complexities involving online and offline calculations as proposed in [15], [20], and [21].

In this paper, an LC-type series resonant DAB converter incorporating a switch-controlled inductor (SCI) is proposed to achieve soft switching for wide-range variations in output voltage and current. ZVS at the primary side (high voltage) and zero current switching (ZCS) at the secondary side (low voltage) are achieved for charging/discharging a 48-V supercapacitor module from a 400-V dc bus. ZCS is preferred over ZVS at the secondary side, where high current flows, to avoid excessive ringing and current surge due to circulating current arising from the out-of-phase relationship between bridge voltage and tank current at the secondary side leading to significant energy stored in parasitic inductances [10], [25]. When designing the proposed converter, conduction loss has been minimized by choosing the nominal operating point that gives the minimum root-mean-square (rms) resonant tank current at the maximum value of output current over the entire range of voltage conversion ratio. In Section II, both the conventional LC-type series resonant DAB converter and the proposed topology based on an SCI are analyzed to identify their ZVS and ZCS conditions. To reduce conduction loss, the design of nominal operating point with the minimum rms tank current is explained in Section III. The design of experimental prototype, simulation, and experimental results for charging/discharging a supercapacitor module are presented in Section IV. Finally, concluding remarks are given in Section V.

II. Analysis of Conventional and Proposed DAB Topology

A. Conventional Topology Based on an LC Series Resonant Tank

A conventional LC-type series resonant DAB converter is shown in Fig. 2. Switches S_1–S_4 form the primary side of the converter and are modulated to generate $v_p(t)$. The secondary side of the converter, which is composed of Q_1–Q_4, generates a phase-shifted $v_s(t)$ as shown in Fig. 4. The magnitude and direction of power flow are determined by the phase shift θ between $v_p(t)$ and $v_s'(t)$. Power is assumed to be transferred by the fundamental components of the resonant tank current and bridge voltages, which leads to simplified analytical expressions of results [23]. Therefore, FCA is used to determine the converter's behavior, and an equivalent circuit along with the corresponding phasor diagrams showing the voltages and currents of interest are shown in Fig. 3. The respective equations for the primary-reflected resonant tank current and bridge voltages are given by (1)–(3)

$$v_p(t) = \frac{4V_p}{\pi}\sin\omega t \tag{1}$$

$$v_s^{'}(t) = \frac{4MV_p}{\pi}\sin(\omega t-\theta) \tag{2}$$

$$i_p(t) = \frac{4V_p}{\pi X}(-\cos\omega t + M\cos(\omega t-\theta)) \tag{3}$$

where $M=\frac{nV_s}{V_p}$, $X=\omega L-\frac{1}{\omega C}$, θ is the phase shift between $v_p(t)$ and $v_s^{'}(t)$, and n is the transformer's turn ratio.

1) Required Soft-Switching Conditions: From Fig. 2, in order to achieve ZVS operation during the switching instances of

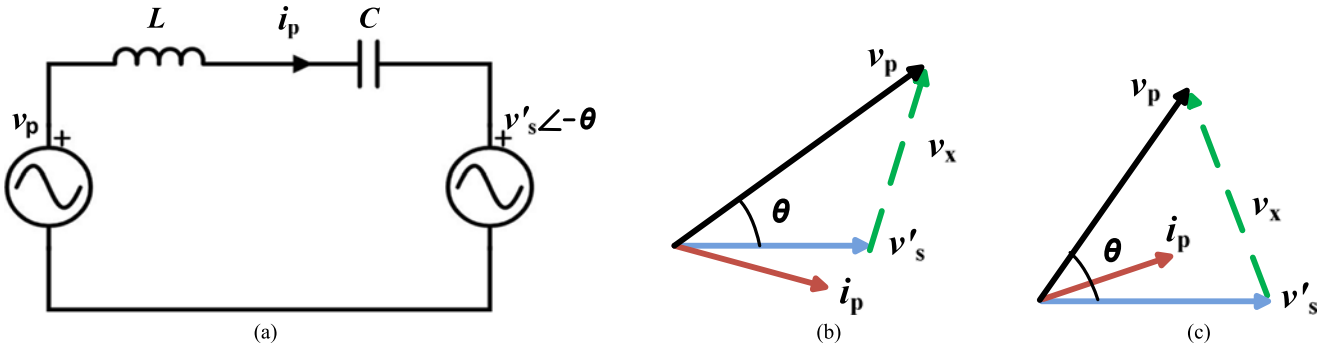

Fig. 3. (a) Equivalent circuit of the conventional DAB converter. (b) Phasor representation for hard switching. (c) Phasor representation for soft switching.

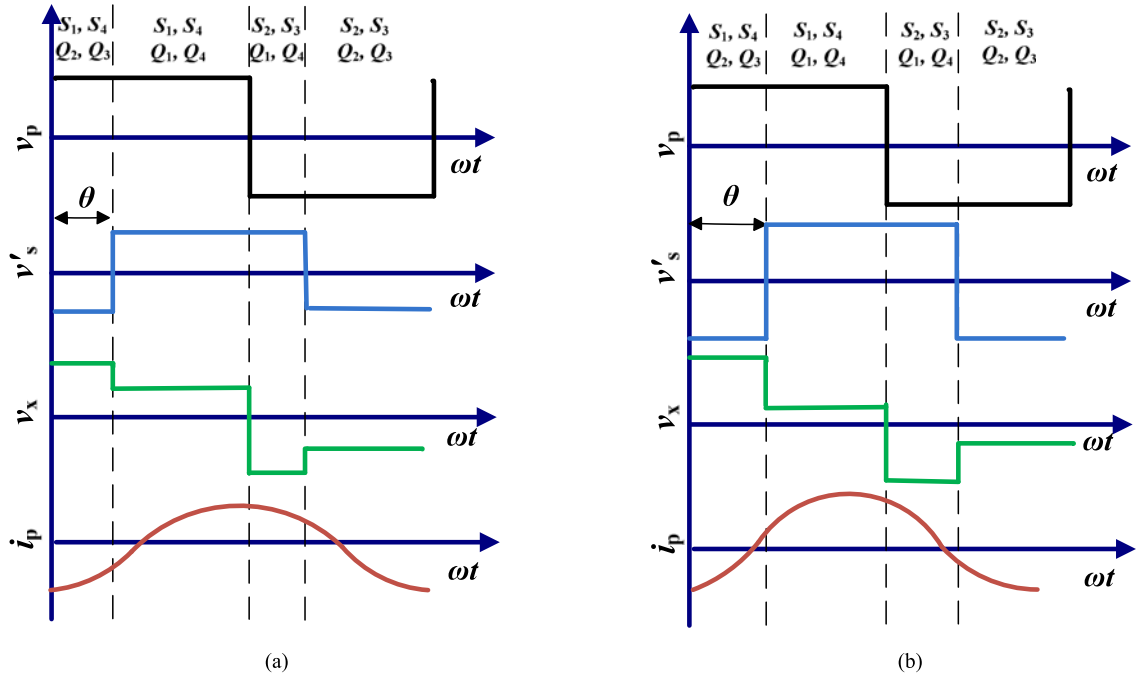

Fig. 4. Operating waveforms of the DAB converter based on an LC-type series resonant tank. (a) Hard switching. (b) Soft switching.

S_1 and S_4, the corresponding body diodes should conduct before S_1 and S_4 are turned ON, implying that $i_p(t)$ must be negative when S_1 and S_4 are turned ON. As for the secondary side, $i_p(t)$ must be positive to achieve ZVS and zero for ZCS when Q_1 and Q_4 are turned ON. Similarly, for S_2 and S_3, $i_p(t)$ should be positive, and negative or zero for Q_2 and Q_3. Operating waveforms depicting hard-switching and soft-switching behavior of the conventional DAB converter are shown in Fig. 4. Thus, evaluating (3) at $\omega t = 0$ (i.e., when S_1 and S_4 are turned ON) and θ (i.e., when Q_1 and Q_4 are turned ON) lead to the required conditions for achieving ZVS for the primary-side switches and ZVS/ZCS for the secondary-side switches

$$i_p(0) = \frac{4V_p}{\pi X}(-1 + M\cos\theta) < 0 \Rightarrow \cos\theta < \frac{1}{M} \quad (4)$$

$$i_p\left(\frac{\theta}{\omega}\right) = \frac{4V_p}{\pi X}(-\cos\theta + M) \geq 0 \Rightarrow \theta \geq \cos^{-1} M. \quad (5)$$

On the primary side, the required condition can be met for all $M \leq 1$ by ensuring $\frac{nV_{s(\max)}}{V_p} \leq 1$, but from (5), it can be seen that the secondary-side switches will experience hard switching for wide-range variations in M and θ.

B. Proposed Topology Based on an SCI

The proposed topology of the DAB converter and the corresponding FCA-based equivalent circuit are shown in Figs. 5 and 6, respectively. It can be seen that the SCI is inserted at the secondary side to split the secondary-reflected current $ni_p(t)$ into $i_s(t)$ and $i_{\text{sci}}(t)$, and their relationship is given by

$$i_s(t) = \frac{n4V_p}{\pi X}(-\cos\omega t + M\cos(\omega t - \theta)) - i_{\text{sci}}(t). \quad (6)$$

The general description and working principle of the SCI have been discussed in [26] and operating waveforms illustrating the use of an SCI in the proposed topology are shown Fig. 7. The phase shift β between the voltage across the SCI (i.e., $v_s(t)$) and

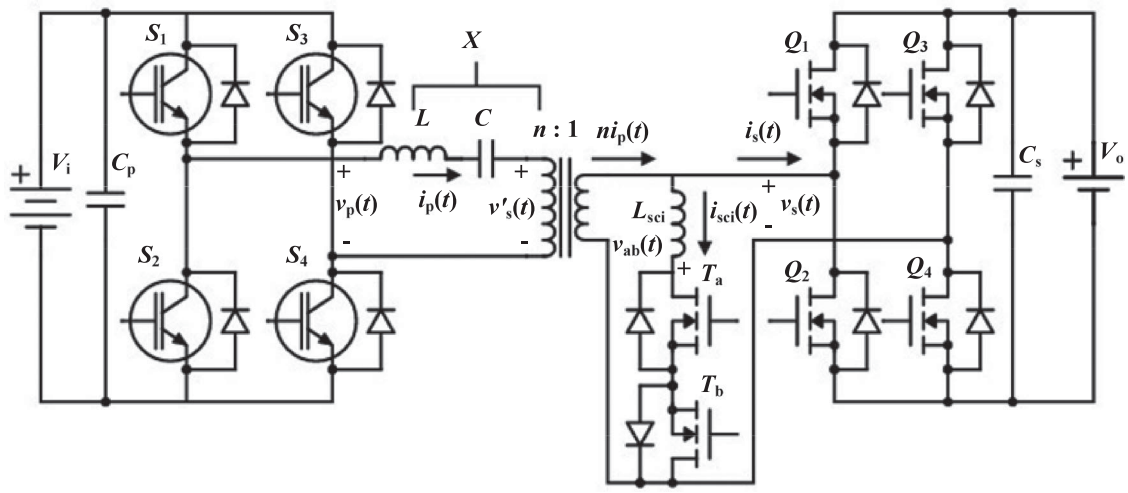

Fig. 5. Proposed topology based on an SCI.

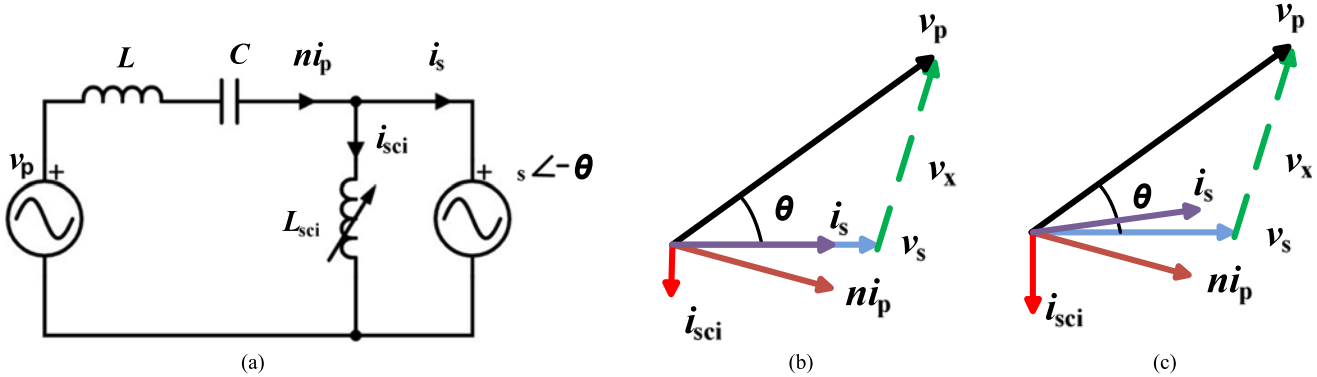

Fig. 6. (a) Equivalent circuit of the proposed DAB converter. (b) Phasor representation for ZCS. (b) Phasor representation for ZVS.

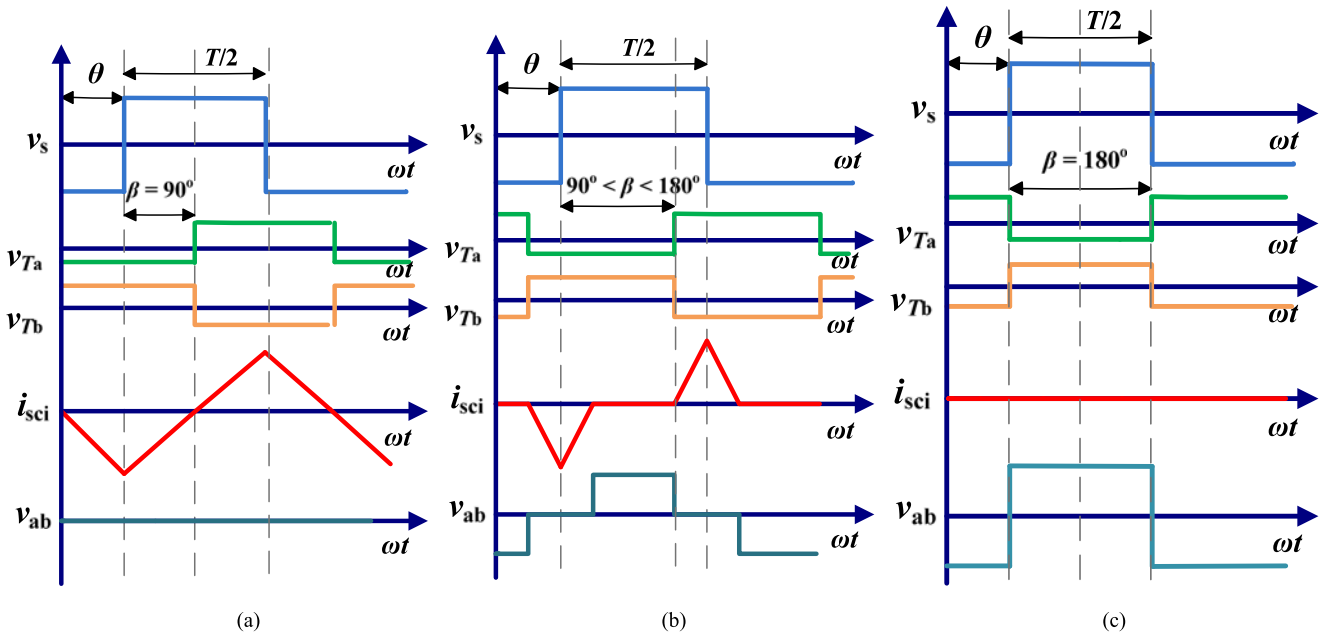

Fig. 7. Operating waveforms of the SCI for its use in DAB converter. (a) Firing-angle $\beta = 90°$. (b) Firing-angle $90° < \beta < 180°$. (c) Firing-angle $\beta = 180°$.

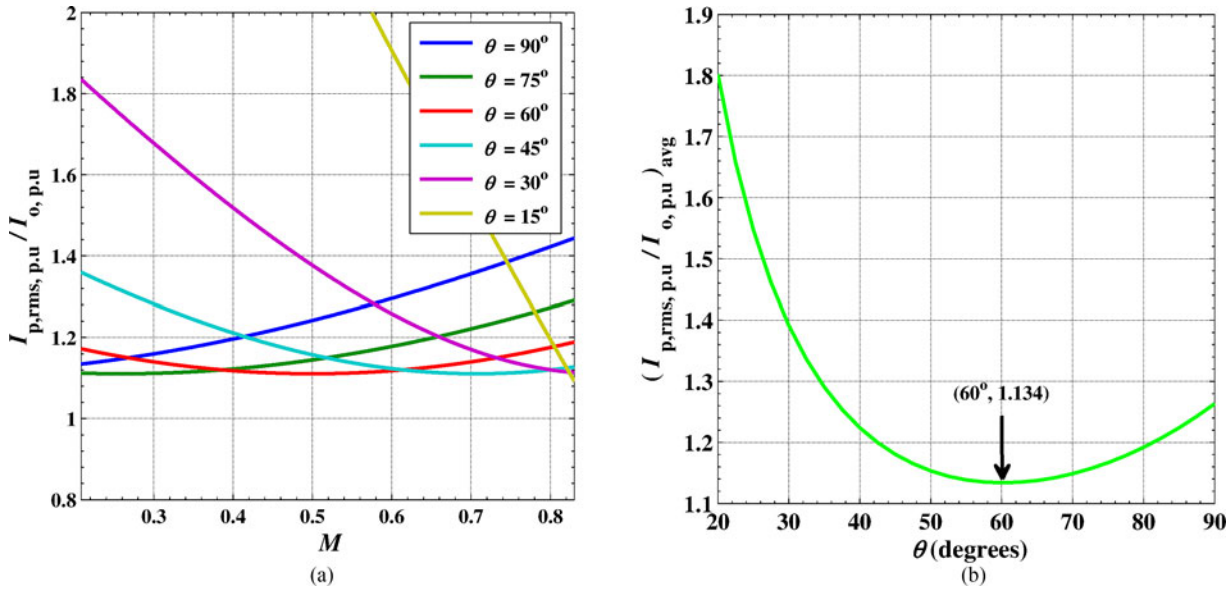

Fig. 8. (a) $I_{\mathrm{p,rms,p.u}}/I_{\mathrm{o,p.u}}$ versus M for different choices of nominal operating points θ. (b) Average values of $I_{\mathrm{p,rms,p.u}}/I_{\mathrm{o,p.u}}$ versus θ within given range of M.

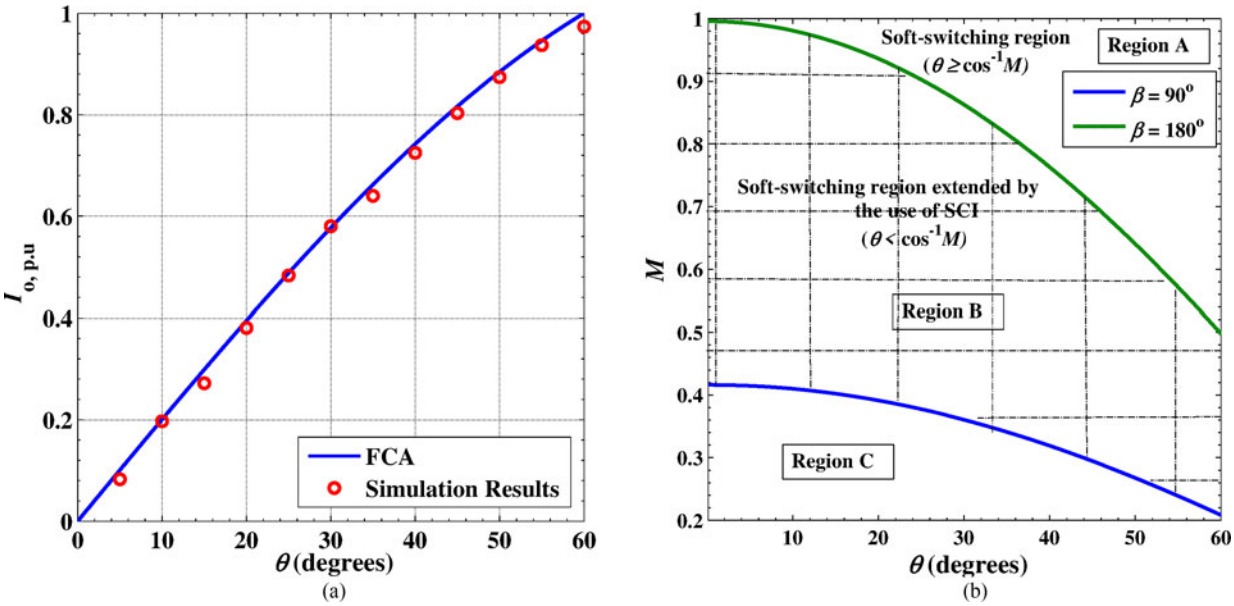

Fig. 9. (a) Variation of the output current $I_{\mathrm{o,p.u}}$ with respect to change from nominal operating point θ. (b) Operating region of the proposed DAB converter's topology.

the driving signal for T_a determines the effective inductance, and hence, the current $i_{\mathrm{sci}}(t)$ flowing through L_{sci}. Setting $\beta = 90^\circ$ gives the maximum $i_{\mathrm{sci}}(t)$ and minimum effective effective inductance of L_{sci} and at $\beta = 180^\circ$ SCI becomes inactive with $i_{\mathrm{sci}}(t) = 0$ and $L_{\mathrm{sci}} \to \infty$.

1) Required Soft-Switching Conditions: The required condition to achieve ZVS at the primary side would remain the same, whereas the condition for achieving ZVS/ZCS at the secondary side is given by

$$i_s\left(\frac{\theta}{\omega}\right) = \frac{n4V_p}{\pi X}(-\cos\theta + M) - I'_{\mathrm{sci}} \geq 0 \tag{7}$$

where I'_{sci} is the peak value of the current flowing through SCI, which occurs at the zero crossing of $v_s(t)$ (i.e., $t = \frac{\theta}{\omega}$) and is given by

$$I'_{\mathrm{sci}} = \frac{V_s}{2\pi f L_{\mathrm{sci}}}(\beta - \pi) \tag{8}$$

where T is the switching period.

The required β to achieve ZVS/ZCS is given by (9) and the corresponding phasor diagrams are shown in Fig. 6

$$\beta \leq \frac{8n^2 f L_{\mathrm{sci}}}{X} - \frac{8n^2 f L_{\mathrm{sci}}\cos\theta}{MX} + \pi. \tag{9}$$

TABLE I
SPECIFICATIONS OF THE CONVERTER PROTOTYPE

Input voltage V_i	400 V
Output voltage V_o	10–48 V
Transformer ratio n	8.3
Proposed resonant tank (L, C, and $L_{\rm sci}$)	(753 μH, 6.6 nF, and 4.71 μH)
Switching frequency f_s	100 kHz
Maximum rated output current I_o	10 A
Maximum rated output power $P_{\rm avg,o}$	480 W
Primary-side IGBTS	STGW19NC60WD (600 V, 19 A)
Secondary-side and SCI MOSFETs	FDPF085N10A (100 V, 40 A, 6.5 mΩ)
Gate drivers	Infineon 2ED020I12-F2
Inductor's core shape and material	FC3 Ferrite (ETD-44 Core)
Transformer's core shape and material	FC3 Ferrite (ETD-44 Core)
Supercapacitor	Maxwell Technologies (48 V, 83 F)
Controller	32-bit ARM Cortex-M3 PSoC 5LP by Cypress Semiconductor
Voltage and current sensors	LEM Sensors (LV25-P and LA55-P)

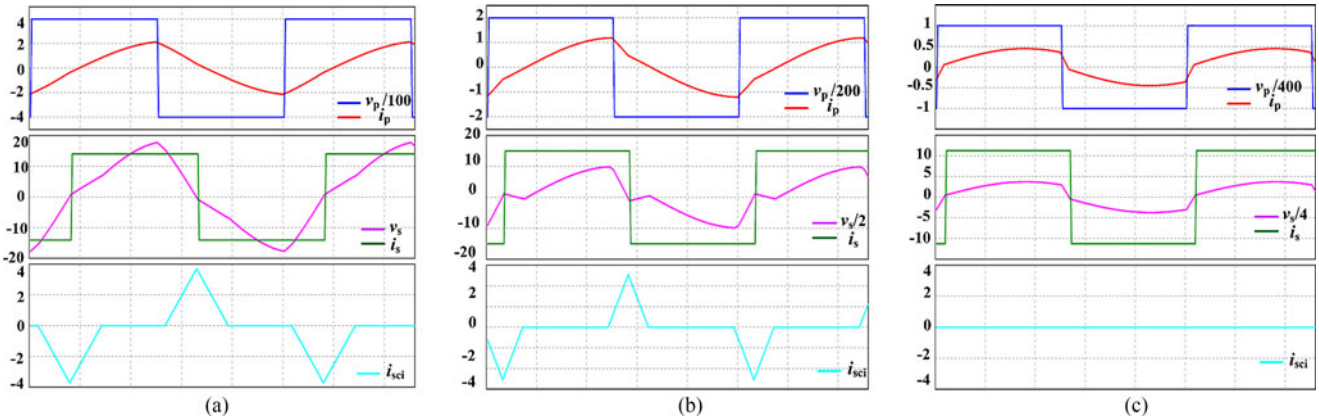

Fig. 10. Simulation results. (a) Charging with $V_p = 400$ V, $V_s = 14$ V, $I_o = 9.75$ A, $M = 0.29$, $\theta = 60°$, $\beta = 134.2°$, $I_{\rm p,rms} = 1.36$ A, $I_{\rm s,rms} = 11.2$ A, and $I_{\rm sci,rms} = 1.25$ A. (b) Charging with $V_p = 400$ V, $V_s = 30$ V, $I_o = 4.83$ A, $M = 0.625$, $\theta = 25.7°$, $\beta = 151.8°$, $I_{\rm p,rms} = 0.77$ A, $I_{\rm s,rms} = 6.13$ A, and $I_{\rm sci,rms} = 1.35$ A. (c) Charging with $V_p = 400$ V, $V_s = 45$ V, $I_o = 2.72$ A, $M = 0.937$, $\theta = 15.1°$, $\beta = 180°$, $I_{\rm p,rms} = 0.36$ A, $I_{\rm s,rms} = 3$ A, and $I_{\rm sci,rms} = 0$ A.

Furthermore, it can be seen from Fig. 7 that the switches T_a and T_b are both turned ON and turned OFF at zero current [26], hence ZCS is always achieved in the SCI switches. The initial fixed value of $L_{\rm sci}$ is obtained from (9) by keeping the SCI's firing angle $\beta = 90°$ at the required minimum M and θ to produce the required output current. More explanation will be given in Section IV.

The selection of the nominal operating θ for the conventional DAB converter lies in the range of 0–90°, but under wide-range variations in the output voltage and current, there is a need to operate with low conduction loss (i.e., minimum rms value of the primary-side resonant tank current under the specified range of M). The selection of nominal operating point θ for reduced conduction loss is discussed in the next section.

III. Design of Nominal Operating Point for Reduced Conduction Loss at Maximum Output Current

In the following analysis, normalized variables (i.e., per-unit values) are used to generalize the results for all power levels. To perform FCA in normalized form, the following base values are used: $V_B = V_p$, $Z_B = n^2(V_o/I_o)$ and $I_B = V_B/Z_B$. Equations (10)–(12) give the normalized forms of (1)–(3) for a generalized analysis

$$v_{\rm p,p.u}(t) = \frac{4}{\pi}\sin\omega t \tag{10}$$

$$v'_{\rm s,p.u}(t) = \frac{4M}{\pi}\sin(\omega t - \theta) \tag{11}$$

$$i_{\rm p,p.u}(t) = \frac{4}{\pi X_{p.u}}(-\cos\omega t + M\cos(\omega t - \theta)) \tag{12}$$

where $X_{\rm p.u} = X/Z_B$.

The rms value of the primary-side resonant tank current $i_{\rm p,p.u}(t)$ is derived from (12) by setting its first derivative to zero and dividing the peak tank current by $\sqrt{2}$, and the result is given by

$$I_{\rm p,rms,p.u} = \frac{4}{\pi X_{\rm p.u}\sqrt{2}}(-\cos\omega_p t_p + M\cos(\omega_p t_p - \theta)) \tag{13}$$

where $\omega_p t_p$ is given by

$$\omega_p t_p = \tan^{-1}\left(\frac{-M\sin\theta}{1 - M\cos\theta} + \pi\right). \tag{14}$$

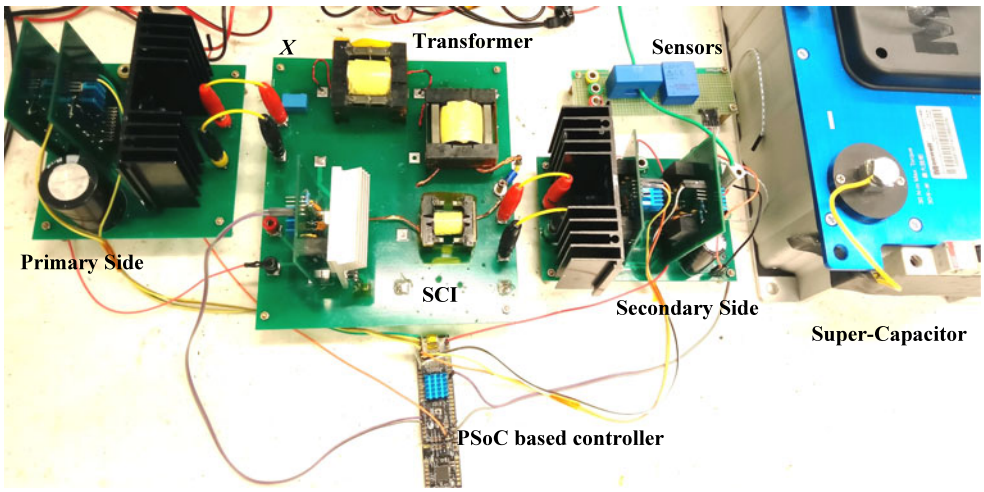

Fig. 11. Hardware realization of the proposed DAB converter topology.

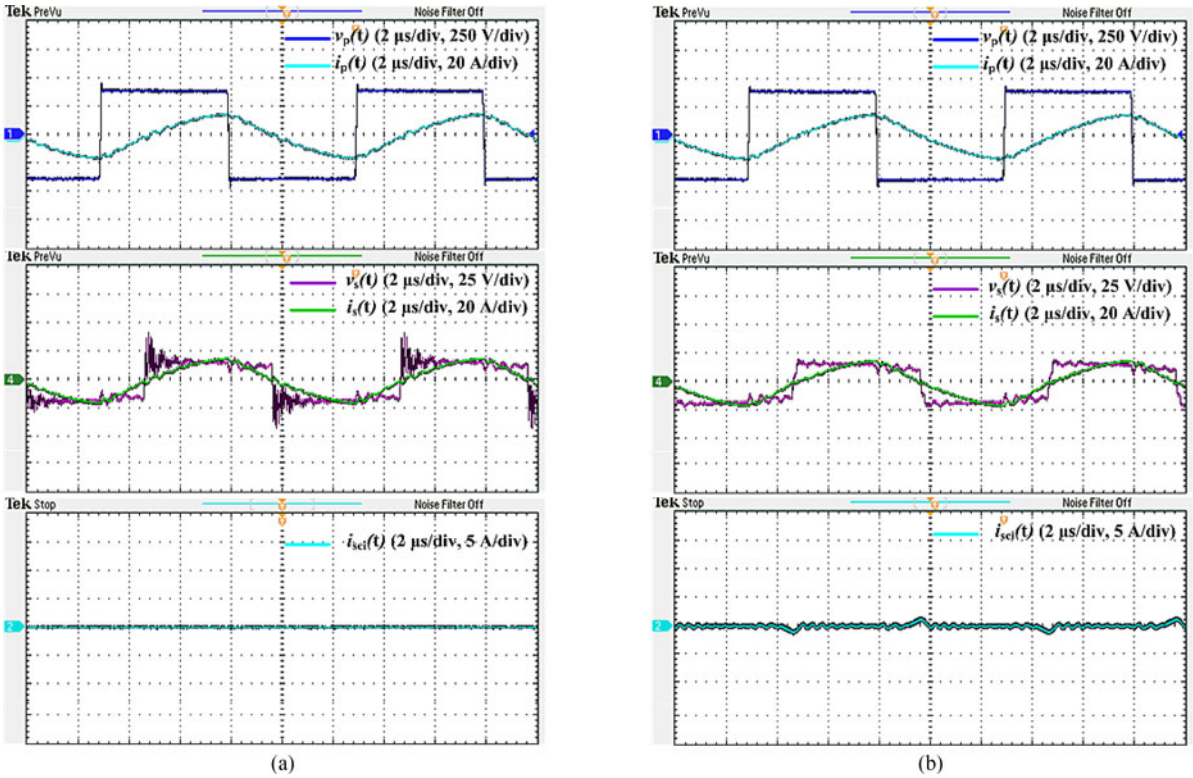

Fig. 12. Experimental results for charging at $V_p = 400$ V, $V_s = 14$ V, $I_o = 9.30$ A, $M = 0.29$, and $\theta = 60°$. (a) Without SCI, efficiency $= 77.9\%$, $I_{\mathrm{p,rms}} = 10.2$ A, $I_{\mathrm{s,rms}} = 10.1$ A, and $I_{\mathrm{sci,rms}} = 0$ A. (b) With SCI, $\beta = 133.8°$, efficiency $= 78.5\%$, $I_{\mathrm{p,rms}} = 10.3$ A, $I_{\mathrm{s,rms}} = 10.2$ A, $I_{\mathrm{sci,rms}} = 0.35$ A, and total power loss of SCI $P_{\mathrm{tot,sci}} = 0.5$ W [27], [28].

The instantaneous and average output power being transferred from the primary side to the secondary side of the DAB converter can be evaluated from either side of the resonant tank and the results are given by

$$\begin{aligned} P_{\mathrm{int,p.u}}(t) &= v_{\mathrm{p,p.u}}(t) i_{\mathrm{p,p.u}}(t) \\ &= \frac{-16}{\pi^2 X_{\mathrm{p.u}}} (\sin \omega t \cos \omega t - M \sin \omega t \cos(\omega t - \theta)) \end{aligned} \tag{15}$$

$$\begin{aligned} P_{\mathrm{avg,p.u}} &= \frac{1}{2\pi} \int_0^{2\pi} v_{\mathrm{p,p.u}}(t) i_{p,p.u}(t) \\ &= \frac{8M}{\pi^2 X_{\mathrm{p.u}}} \sin \theta. \end{aligned} \tag{16}$$

The rated per-unit output current $I_{\mathrm{o,p.u}}$ can also be obtained from (16) by dividing the per-unit average output power by the per-unit output voltage. It can be seen from (17) that $I_{\mathrm{o,p.u}}$ is

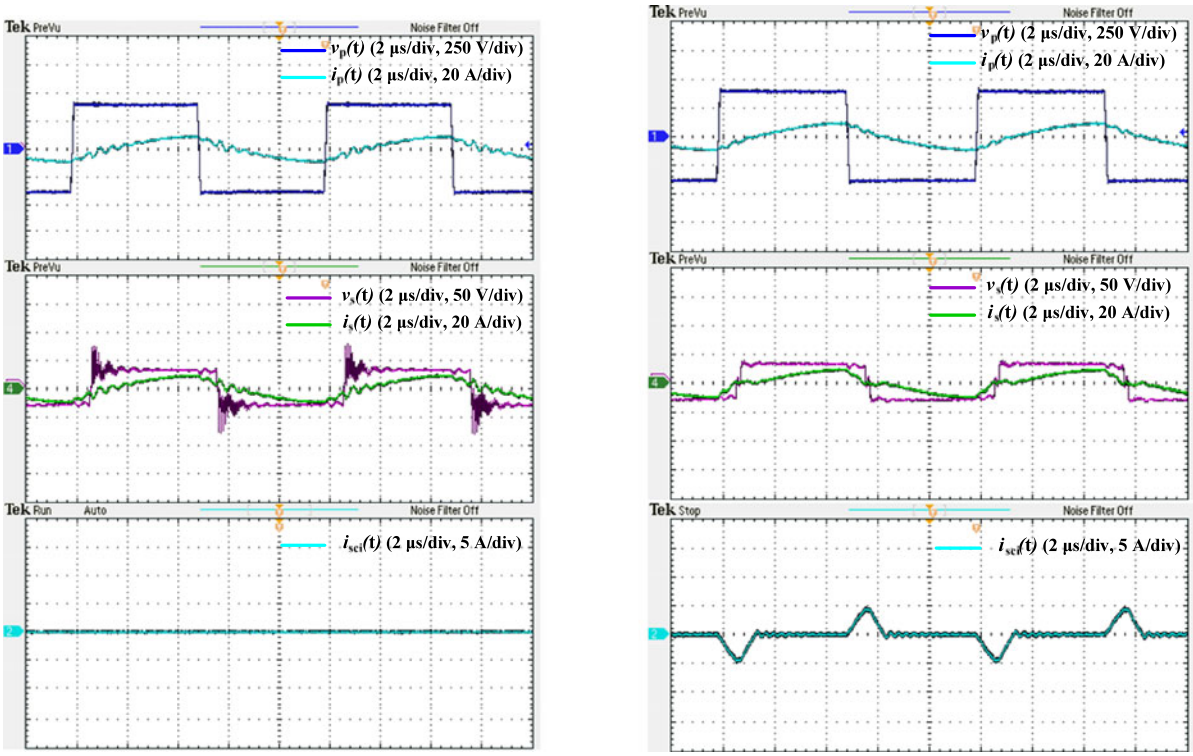

Fig. 13. Experimental results for charging at $V_p = 400$ V, $V_s = 30$ V, $I_o = 4.9$ A, $M = 0.625$, and $\theta = 26°$. (a) Without SCI, efficiency $= 88.73\%$, $I_{p,rms} = 6.03$ A, $I_{\mathrm{s,rms}} = 6.05$ A, and $I_{\mathrm{sci,rms}} = 0$ A. (b) With SCI, $\beta = 150°$, efficiency $= 90.38\%$, $I_{\mathrm{p,rms}} = 6.21$ A, $I_{\mathrm{s,rms}} = 5.96$ A, $I_{\mathrm{sci,rms}} = 1.55$ A, and total power loss of SCI $P_{\mathrm{tot,sci}} = 1.6$ W [27], [28].

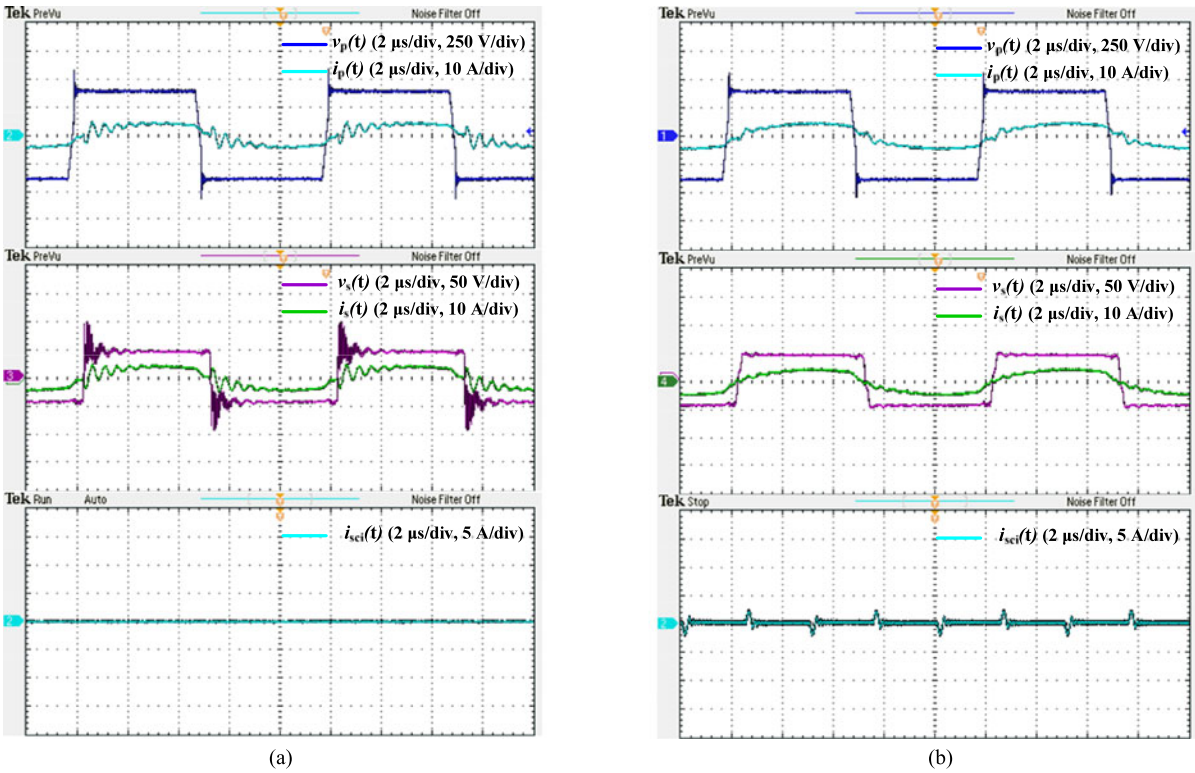

Fig. 14. Experimental results for charging at $V_p = 400$ V, $V_s = 45$ V, $I_o = 3.1$ A, $M = 0.937$, and $\theta = 16.6°$. (a) Without SCI, efficiency $= 91.80\%$, $I_{\mathrm{p,rms}} = 3.40$ A, $I_{\mathrm{s,rms}} = 3.41$ A, and $I_{\mathrm{sci,rms}} = 0$ A. (b) With SCI, $\beta = 175°$, efficiency $= 94.3\%$, $I_{\mathrm{p,rms}} = 3.50$ A, $I_{\mathrm{s,rms}} = 3.47$ A, $I_{\mathrm{sci,rms}} = 0.33$ A, and total power loss of SCI $P_{\mathrm{tot,sci}} = 0.49$ W [27], [28].

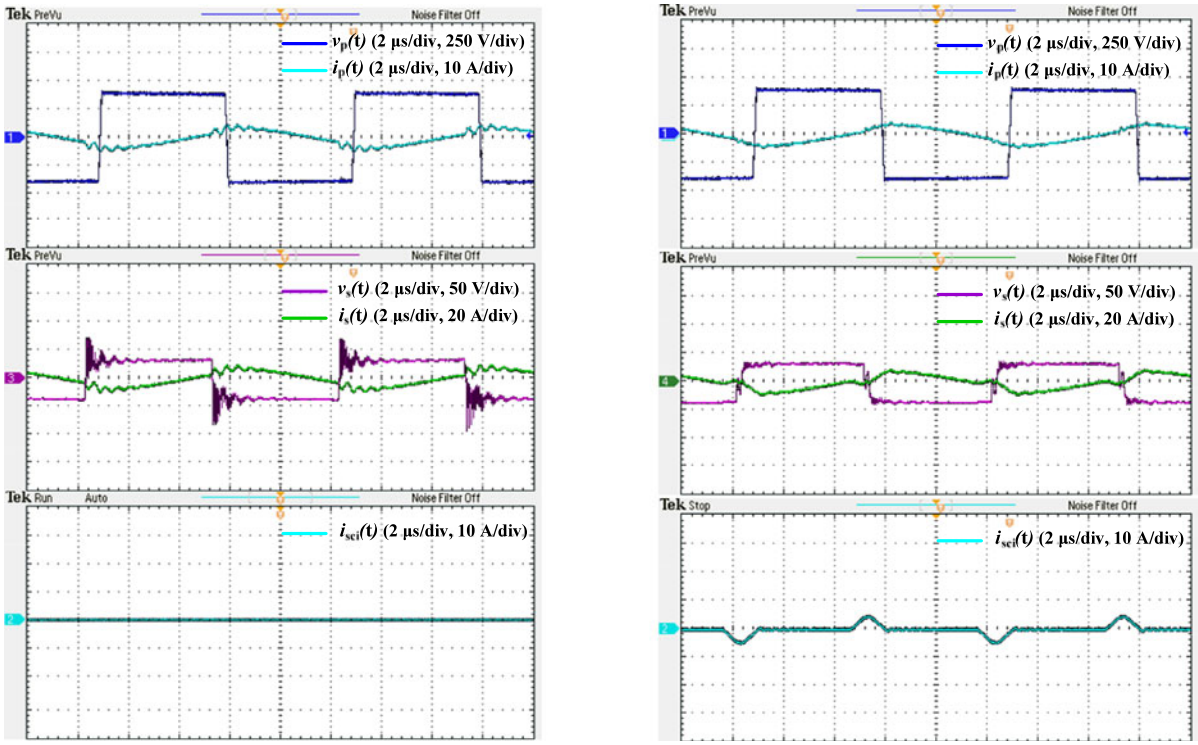

Fig. 15. Experimental results for discharging at $V_p = 400$ V, $V_s = 35$ V, $I_o = 4.0$ A, $M = 0.73$, and $\theta = -22.0°$. (a) Without SCI, efficiency $= 90.25\%$, $I_{\mathrm{p,rms}} = 5.01$ A, $I_{\mathrm{s,rms}} = 5.02$ A, and $I_{\mathrm{sci,rms}} = 0$ A. (b) With SCI, $\beta = 155°$, efficiency $= 91.57\%$, $I_{\mathrm{p,rms}} = 5.07$ A, $I_{\mathrm{s,rms}} = 4.70$ A, $I_{\mathrm{sci,rms}} = 1.59$ A, and total power loss of SCI $P_{\mathrm{tot,sci}} = 1.63$ W [27], [28].

independent of the output voltage

$$I_{\mathrm{o,p.u}} = \frac{8}{\pi^2 X_{\mathrm{p.u}}} \sin\theta. \tag{17}$$

In the proposed topology, the impedance $X_{\mathrm{p.u}}$ is fixed, M is dependent on the output voltage, and θ is used to control the output current. The per-unit rms tank current $I_{\mathrm{p,rms,p.u}}$ expressed in terms of $I_{\mathrm{o,p.u}}$ can be evaluated by substituting $X_{\mathrm{p.u}}$ from (17) into (13) and the result is given by

$$\frac{I_{\mathrm{p,rms,p.u}}}{I_{\mathrm{o,p.u}}} = \frac{\pi}{2\sqrt{2}\sin\theta}(-\cos\omega_p t_p + M\cos(\omega_p t_p - \theta)). \tag{18}$$

From (18), the normalized behavior of $I_{\mathrm{p,rms,p.u}}/I_{\mathrm{o,p.u}}$ with respect to variations in M can now be analyzed and their quantitative relationship is plotted in Fig. 8(a) using (18). Again the normalization ensures that the result and any conclusion that it leads to will hold for all power levels. It is apparent from Fig. 8(a) that a desired nominal operating point with reduced conduction loss can be chosen by identifying the value of θ that gives the minimum average value of $I_{\mathrm{p,rms,p.u}}/I_{\mathrm{o,p.u}}$ over a given range of M, as shown in the following equation:

$$\left(\frac{I_{\mathrm{p,rms,p.u}}}{I_{\mathrm{o,p.u}}}\right)_{\mathrm{avg}} = \frac{1}{M_{\max} - M_{\min}} \int_{M_{\min}}^{M_{\max}} \frac{I_{\mathrm{p,rms,p.u}}}{I_{\mathrm{o,p.u}}} dM. \tag{19}$$

IV. Simulation and Experimental Results

In order to verify the feasibility of the proposed idea, a DAB converter based on an SCI is designed to charge/discharge a supercapacitor with a variation of M from 0.208 to 0.83. The nominal operating point with reduced conduction loss over the given range of M can be obtained by plotting (19) against different values of θ as shown in Fig. 8(b) and such an operating point is identified to be that with $\theta = 60^{\mathrm{o}}$ or 1.047 rad. Hence, $\theta = 60^{\mathrm{o}}$ is used to calculate the value of $X_{\mathrm{p.u}}$ required to deliver the maximum rated per-unit output current. From (17), the desired value of $X_{\mathrm{p.u}}$ is 0.7019 Ω and using this value of $X_{\mathrm{p.u}}$, the variation of the per-unit output current with respect to θ is plotted using (17) and is shown in Fig. 9(a). It can be seen that the maximum value of $I_{\mathrm{o,p.u}}$ occurs at the selected nominal operating point and θ should be decreased to reduce the output current, which is usually needed when it is required to charge/discharge supercapacitor slowly or as its voltage approaches the rated maximum value (i.e., 48 V). Fig. 9(a) also compares the output current calculated using (17) to that generated by circuit simulation, where the actual current waveform is considered. The close agreement between the two results implies that the error incurred by applying FCA is small and power is mainly transferred by the fundamental component of the tank current.

The specifications of the proposed topology are given in Table I based on which the required base values are $V_B = 400$ V and $Z_B = n^2(V_o^2/P_o) = 330.67$ Ω. The equivalent impedance

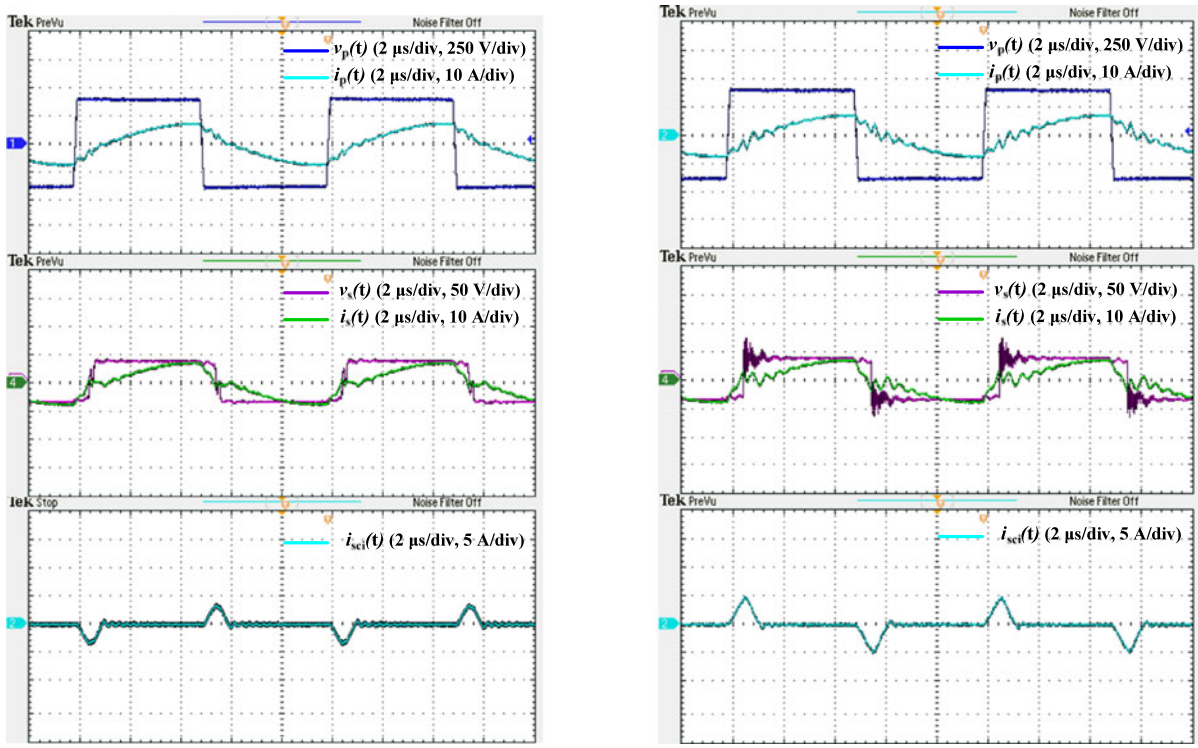

Fig. 16. Experimental results for charging at $V_p = 400$ V, $V_s = 35$ V, $I_o = 4.2$ A, $M = 0.73$, and $\theta = 20.2°$. (a) ZCS, $\beta = 161°$, efficiency $= 92.40\%$, $I_{\mathrm{p,rms}} = 5.04$ A, $I_{\mathrm{s,rms}} = 4.91$ A, and $I_{\mathrm{sci,rms}} = 0.97$ A. (b) ZVS, $\beta = 154°$, efficiency $= 90.80\%$, $I_{\mathrm{p,rms}} = 5.04$ A, $I_{\mathrm{s,rms}} = 4.89$ A, $I_{\mathrm{sci,rms}} = 1.44$ A, and total power loss of SCI $P_{\mathrm{tot,sci}} = 1.5$ W [27], [28].

of the LC series resonant tank is $X = X_{\mathrm{p.u}} Z_B = 232.1\ \Omega$. The value of L_{sci} is chosen to be 4.71 μH with $M = 0.2083$ ($V_o = 10$ V) at the maximum rated output current of $I_o = 10$ A and $\beta = 90°$.

The hard-switching region covered by the chosen L_{sci} is shown in Fig. 9(b) plotted using (9) and the Region A above the green curve undergoes soft switching by naturally meeting the required condition of (5). The relatively small adjustable Region C (i.e., depends on L_{sci}) under the gridded Region B corresponds to the low output current I_o at low voltage that is not covered by the SCI designed previously as supercapacitor does not typically operate in this region and ZCS can be triggered with the aid of the energy stored in the MOSFETs' parasitic inductances during hard-switching operation at low output voltages [9]. During hard switching at low voltages, there will still be ringing due to reverse recovery effects but the losses are relatively low because of small reverse recovery charge and parasitic inductances limit the slew rate of the currents through the secondary-side MOSFETs as shown in Fig. 12 [9], [10]. If needed the value of L_{sci} can be redesigned to extend the soft-switching region to Region C at the expense of increased I_{sci}, and hence, conduction loss in the SCI switches.

A. Simulation Results

The proposed DAB converter is simulated using PSIM and the main operating waveforms are shown in Fig. 10. Fig. 10(a) corresponds to the case of charging the supercapacitor at a voltage of 14 V with the maximum rated output current of 10 A, while Fig. 10(b) and (c) represents the cases of charging with reduced output current as the supercapacitor's voltage approaches its rated value of 48 V. It is evident that ZVS is achieved for the primary-side switches and ZCS is achieved for the secondary-side switches for the depicted values of M and I_o. It can be seen in Fig. 10(c) that the SCI essentially becomes inactive and $i_p(t)$ becomes identical to $i_s(t)$ as the DAB converter can achieve natural soft switching at increased values of M and I_o by operating in Region A of Fig. 9(b). Under this condition, the proposed SCI-based DAB converter reverts to the conventional LC-type series resonant DAB converter with the SCI's firing-angle β approaching 180°, the effective inductance L_{sci} approaching ∞ and $i_{\mathrm{sci}}(t)$ tending to zero as shown in Fig. 10(c).

B. Experimental Results

The hardware prototype of the proposed SCI-based DAB converter topology with the specifications given by Table I is shown in Fig. 11. The primary-side or high-voltage-side switches are realized by IGBTs, and MOSFETs are used for the secondary-side or low-voltage-side switches. Programmable system-on-chip (PSoC) is used to generate the required pulsewidth modulation signals for the switches and to adjust the firing angle of SCI based on the sensed output voltage and current. The measured waveforms of $v_p(t), v_s(t), i_p(t), i_s(t)$, and $i_{\mathrm{sci}}(t)$ with SCI and without SCI are shown in Figs. 12–14. Fig. 12 ($M = 0.29$

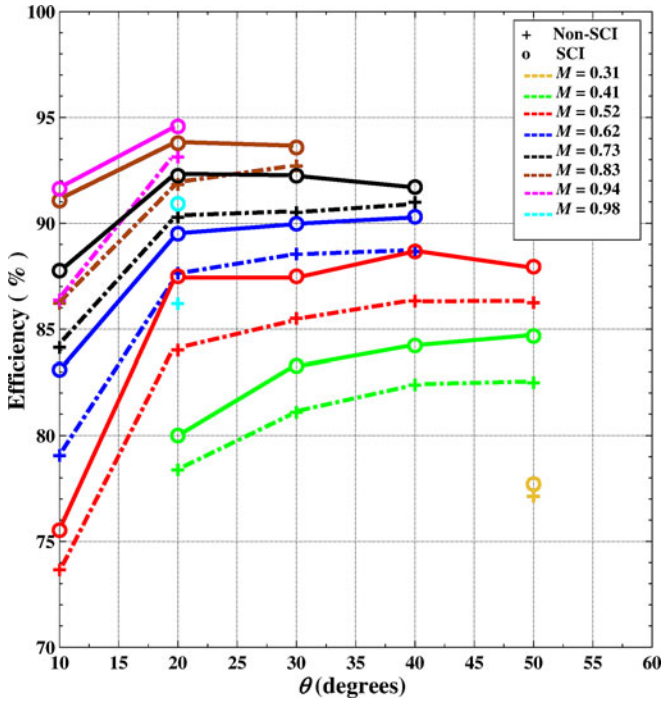

Fig. 17. Measured efficiencies of the DAB converter with and without the use of an SCI at M and θ falling within the conventional hard-switching region (i.e., region B) shown in Fig. 9(b).

and $I_o = 9.30$ A) depicts the case in which the improvement in efficiency by using an SCI is less significant, since at relatively low output voltages, the energy stored in parasitic inductances of the secondary-side MOSFETs are generally large enough to initiate partial ZCS even under the condition of hard switching [9]. A lower efficiency of 91.80% ($M = 0.937$ and $I_o = 3.1$ A) is achieved without the use of an SCI as compared to 94.3% with the use of an SCI and is shown in Fig. 14. As shown in Fig. 13 ($M = 0.625$ and $I_o = 4.9$ A), a higher efficiency of 90.38% is obtained due to the use of an SCI and 88.73% without the use of it. Discharging of the supercapacitor with and without the use of an SCI is given in Fig. 15, which shows the effectiveness of the proposed topology for reverse power flow as well.

The measured waveforms show that ZVS and ZCS are achieved for the primary-side and secondary-side switches, respectively. The reason for avoiding ZVS at the secondary-side switches is to reduce circulating current and parasitic-induced ringing as shown in Fig. 16. The minor difference between the simulated and measured output current I_o is due to the conduction loss caused by the parasitic resistances of semiconductor devices, copper loss, and phase-drift phenomenon caused by the dead-time between two complementary switches in the bridge legs. Converter efficiencies with and without the use of an SCI for the values of M and θ that fall into the conventional hard-switching region are plotted in Fig. 17. The increase in efficiency with increasing M can be explained by the fact that, at lower M, and hence, at lower output power (since the output current is constant and depends on θ only), the conduction loss due to the parasitic resistances of semiconductor devices and PCB traces are constant for a given output current and poses more weight in efficiency as compared to the cases of higher M.

V. Conclusion

DAB converter operating at high frequency can experience significant switching loss due to hard switching. A modified topology of the DAB converter is proposed to achieve ZVS and ZCS for the primary-side and secondary-side switches, respectively, over wide-range variations in the output current and output voltage. The proposed topology utilizes the SCI in such a way that the required ZVS and ZCS conditions are met in the conventional hard-switching region. The nominal operating point is chosen to minimize conduction loss over a wide range of M for improving system's efficiency. To check the feasibility and validity of the proposed topology and its design method, simulation and experimental results at different values of supercapacitor's output voltages and output charging/discharging currents are presented, where a maximum efficiency of 94.6% is obtained.

References

[1] M. Liserre, T. Sauter, and J. Hung, "Future energy systems: Integrating renewable energy sources into the smart power grid through industrial electronics," *IEEE Ind. Electron. Mag.*, vol. 4, no. 1, pp. 18–37, Mar. 2010.

[2] J. Lai and D. J. Nelson, "Energy management power converters in hybrid electric and fuel cells vehicles," *Proc. IEEE*, vol. 95, no. 4, pp. 766–777, Apr. 2007.

[3] R. W. De Doncker, D. M. Divan, and M. H. Kheraluwala, "A three-phase soft-switched high-power-density DC/DC converter for high-power applications," *IEEE Trans. Ind. Appl.*, vol. 27, no. 1, pp. 63–73, Jan./Feb. 1991.

[4] S. Inoue and H. Akagi, "A bidirectional isolated DC–DC converter as a core circuit of the next-generation medium-voltage power conversion system," *IEEE Trans. Power Electron.*, vol. 22, no. 2, pp. 535–542, Mar. 2007.

[5] S. Inoue and H. Akagi, "A bidirectional DC–DC converter for an energy storage system with galvanic isolation," *IEEE Trans. Power Electron.*, vol. 22, no. 6, pp. 2299–2306, Nov. 2007.

[6] B. Zhao, Q. Song, W. Liu, and Y. Sun, "Overview of dual-active bridge isolated bidirectional DC–DC converter for high-frequency-link power-conversion system," *IEEE Trans. Power Electron.*, vol. 29, no. 8, pp. 4091–4106, Aug. 2014.

[7] B. Zhao, Q. Song, W. Liu, and Y. Sun, "A synthetic discrete design methodology of high-frequency isolated bidirectional DC/DC converter for grid-connected battery energy storage system using advanced components," *IEEE Trans. Power Electron.*, vol. 61, no. 10, pp. 5402–5410, Oct. 2014.

[8] X. Li and A. K. S. Bhat, "Analysis and design of high-frequency isolated dual-bridge series resonant DC/DC converter," *IEEE Trans. Power Electron.*, vol. 25, no. 4, pp. 850–862, Apr. 2010.

[9] F. Krismer and J. W. Kolar, "Accurate power loss model derivation of a high-current dual active bridge converter for an automotive application," *IEEE Trans. Ind. Electron.*, vol. 57, no. 3, pp. 881–891, Mar. 2010.

[10] F. Krismer, S. Round, and J. W. Kolar, "Performance optimization of a high current dual active bridge with a wide operating voltage range," in *Proc. 37th IEEE Annu. Power Electron. Spec. Conf.*, Jeju, South Korea, Jun. 2006, pp. 1–7.

[11] L. Xue, M. Mu, D. Boroyevich, and P. Mattavelli, "The optimal design of GaN-based dual active bridge for bi-directional Plug-IN hybrid electric vehicle (PHEV) charger," in *Proc. IEEE Appl. Power Electron. Conf.*, 2015, pp. 602–608.

[12] L. Xue, D. Boroyevich, and P. Mattavelli, "Switching condition and loss modeling of GaN-based dual active bridge converter for PHEV charger," in *Proc. IEEE Appl. Power Electron. Conf.*, 2016 pp. 1315–1322.

[13] B. Zhao, Q. Yu, and W. Sun, "Extended-phase-shift control of isolated bidirectional DC–DC converter for power distribution in micro-grid," *IEEE Trans. Power Electron.*, vol. 27, no. 11, pp. 4667–4680, Nov. 2012.
[14] G. G. Oggier, G. O. Garcia, and A. R. Oliva, "Switching control strategy to minimize dual active bridge converter losses," *IEEE Trans. Power Electron.*, vol. 24, no. 7, pp. 1826–1838, Jul. 2009.
[15] G. G. Oggier, G. O. Garcia, and A. R. Oliva, "Modulation strategy to operate the dual active bridge DC–DC converter under soft switching in the whole operating range," *IEEE Trans. Power Electron.*, vol. 26, no. 4, pp. 1228–1236, Apr. 2011.
[16] N. D. Dinh, N. D. Tuyen, G. Fujita, and M. N. B. Muhtazaruddin, "Investigation of ZVS condition for dual-active-bridge converter using dual-phase-shift modulation," in *Proc. IEEE PES Asia-Pacific Power Energy Eng. Conf.*, 2014, pp. 1–6.
[17] H. Bai and C. Mi, "Eliminate reactive power and increase system efficiency of isolated bidirectional dual-active-bridge DC–DC converters using novel dual-phase-shift control," *IEEE Trans. Power Electron.*, vol. 23, no. 6, pp. 2905–2914, Nov. 2008.
[18] B. Zhao, Q. Yu, and W. Sun, "Power characterization of isolated bidirectional dual-active-bridge DC–DC converter with dual-phase-shift control," *IEEE Trans. Power Electron.*, vol. 27, no. 9, pp. 4172–4176, Sep. 2012.
[19] B. Zhao, Q. Yu, and W. Sun, "Efficiency characterization and optimization of isolated bidirectional DC–DC converter based on dual-phase-shift control for DC distribution application," *IEEE Trans. Power Electron.*, vol. 28, no. 4, pp. 1711–1727, Apr. 2013.
[20] F. Krismer and J. W. Kolar, "Efficiency-optimized high-current dual active bridge converter for automotive applications," *IEEE Trans. Ind. Electron.*, vol. 59, no. 7, pp. 2745–2760, Jul. 2012.
[21] F. Krismer and J. W. Kolar, "Closed form solution for minimum conduction loss modulation of DAB converters," *IEEE Trans. Power Electron.*, vol. 27, no. 1, pp. 174–188, Jan. 2012.
[22] L. Corradini, D. Seltzer, D. Bloomquist, R. Zane, D. Maksimovi, and B. Jacobson, "Minimum current operation of bidirectional dual-bridge series resonant DC/DC converters," *IEEE Trans. Power Electron.*, vol. 27, no. 7, pp. 3266–3276, Jul. 2012.
[23] W. Choi, K. M. Rho, and B. H. Cho, "Fundamental duty modulation of dual-active-bridge converter for wide-range operation," *IEEE Trans. Power Electron.*, vol. 31, no. 6, pp. 4048–4064, Jun. 2016.
[24] B. Zhao, Q. Song, W. Liu, and Y. Sun, "Universal high-frequency-link characterization and practical fundamental-optimal strategy for dual-active-bridge DC–DC converter under PWM plus phase-shift control," *IEEE Trans. Power Electron.*, vol. 30, no. 12, pp. 6488–6494, Dec. 2015.
[25] T. Hirose, M. Takasaki, and Y. Ishizuka, "A power efficiency improvement technique for a bidirectional dual active bridge DC–DC converter at light load," *IEEE Trans. Ind. Appl.*, vol. 50, no. 6, pp. 4047–4055, Nov./Dec. 2014.
[26] W. J. Gu and K. Harada, "A new method to regulate resonant converters," *IEEE Trans. Ind. Appl.*, vol. 3, no. 4, pp. 430–439, Oct. 1988.
[27] D. D. Graovac, M. Purschel, and A. Kiep, "MOSFET power losses calculation using the data-sheet parameters," Dec. 2012. [Online]. Available: http://application-notes.digchip.com/070/70-41484.pdf
[28] R. Erickson and D. Maksimovic, "Transformer design," in *Fundamentals of Power Electronics*, 2nd ed. New York, NY, USA: Kluwer, 2004, pp. 582–583.

M. Yaqoob (S'16) received the B.Eng. degree in electronics engineering from the National University of Sciences and Technology, Islamabad, Pakistan, in 2012, and the M.Sc. degree in electric power system and its automation from the North China Electric Power University, Beijing, China, in 2014. He is currently working toward the Ph.D. degree in the area of power electronics with The Hong Kong Polytechnic University, Hong Kong.

His current research interests include high-frequency medium-voltage power conversion systems, bidirectional isolated dc/dc converters and advanced soft-switching techniques.

Mr. Yaqoob serves as a reviewer of the IEEE TRANSACTIONS ON POWER ELECTRONICS, the IEEE TRANSACTIONS ON CONTROL SYSTEMS TECHNOLOGY, and *IET Power Electronics*.

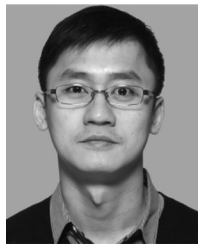

K. H. Loo (S'97–M'99) received the B.Eng. (Hons.) degree in electronic engineering and the Ph.D. degree in electronics engineering from the University of Sheffield, Sheffield, U.K., in 1999 and 2002, respectively.

From 2002 to 2004, he was the Japan Society for the Promotion of Science Postdoctoral Fellow at the Ehime University, Matsuyama, Japan. In 2006, he joined the Faculty of Engineering, Hong Kong Polytechnic University, Hong Kong, as an Instructor,where he is currently an Assistant Professor in the Department of Electronic and Information Engineering. His research interests include power electronics for LED lighting and renewable energy systems.

He has been an Associate Editor for the IEEE TRANSACTIONS ON ENERGY CONVERSION since 2013.

Y. M. Lai (M'92–SM'11) received the B.Eng. degree in electrical engineering from the University of Western Australia, Perth, Australia, in 1983, the M.Eng.Sc. degree in electrical engineering from University of Sydney, Sydney, Australia, in 1986, and the Ph.D. degree in power electronics from Brunel University, London, U.K., in 1997.

He is an Associate Professor with Hong Kong Polytechnic University, Hong Kong. His research interests include computer-aided design of power electronics and nonlinear dynamics.